DOI: 10.24850/j-tyca-2019-06-05
Articles

Geometric optimization of a submerged lens for wave energy focusing

Optimización geométrica de un lente sumergido para focalizar la energía del oleaje

Santiago Gajá[1]
Edgar Mendoza[2]
Rodolfo Silva[3]

[1]Instituto de Ingeniería, División Ambiental, AECOM México - DCS Americas, Mexico City, México, santiago-gaja@aecom.com

[2]Engineer Institute, Universidad Nacional Autónoma de México, Mexico City, Mexico, emendozab@iingen.unam.mx, ORCID: 0000-0002-1991-4721.

[3]Engineer Institute, Universidad Nacional Autónoma de México, Mexico City, Mexico, rsilvac@iingen.unam.mx, ORCID: 0000-0003-0064-9558.

Correspondence author: Edgar Mendoza, emendozab@iingen.unam.mx

Abstract

In this paper, the use of submerged structures of elliptical form are proposed as a viable alternative to focusing of the swell and with it to have high energy sources for its use as a source of renewable energy. A numerical model, validated with experimental data, was used to determine the optimal geometry of the submerged elliptical structure in terms of the length and direction of the incident wave. The results allow the design of the submerged elliptical lenses to function in local hydrodynamic conditions to obtain maximum performance and offer metrics of their efficiency for different geometries in terms of their eccentricity, height, and depth of installation.

Keywords: CELERIS, energy focalization, submerged lenses, wave energy.

Resumen

En este trabajo se propone el uso de estructuras sumergidas de forma elíptica como una alternativa viable para la focalización del oleaje y con ello disponer de focos de alta energía para su aprovechamiento como fuente de energía renovable. Se empleó un modelo numérico, validado con datos experimentales, para determinar la geometría óptima de la estructura elíptica sumergida en términos de la longitud y dirección del oleaje incidente. Los resultados permiten diseñar lentes elípticos sumergidos como función de las condiciones hidrodinámicas locales para obtener su máximo desempeño, y ofrece métricas de su eficiencia para distintas geometrías en términos de su excentricidad, altura, y profundidad de instalación.

Palabras clave: CELERIS, focalización de energía, lentes sumergidos, energía del oleaje.

Received: 15/01/2018

Accepted: 27/05/2019

Introduction

The efficiency of submerged lenses to focus wave energy has been studied by mathematicians and engineers for more than 30 years. Various geometric shapes have been analyzed to evaluate their ability to amplify the waves in a determined, or focal, point and thus provide a useful tool in terms of energy capture and coastal protection.

The first theoretical and experimental studies involved a Fresnel-type lens to produce a non-uniform phase change in a diverging wave to transform it into a converging wave (Mehlum & Stamnes, 1987; Stamnes, Lovhaugen, Spjelkavik, Chiang, & Yue, 1983). Murashige and Kinoshita (1992), made a comparative study between a Fresnel lens and a biconvex lens, both using a profile constructed of small cylinders to reduce the effects of wave reflection. The results showed that biconvex lenses have a better performance than Fresnel lenses, and that using an arrangement of small cylinders as a profile improves efficiency.

A more recent investigation, with more significance to the present project, was the comparative numerical study on the efficiency of a biconvex lens and an elliptical lens, by Griffiths and Porter (2011). In this work, a region of shading around the lenses was included to reduce the effect of diffraction that contributes negatively in the focusing process. The refraction theory was used in conics, to obtain a controlled and predictive targeting process, as this theory establishes that any beam of light that falls parallel to the optical axis of an ellipsoid with a refractive index inverse to the eccentricity $(n = 1/e)$,, will focus on the second geometrical focus of the ellipsoid. The authors used the relationship between the wave number and the refractive index to make use of this principle so that $n = k_2/k_1 = 1/e$, where n is the refractive index and y $k_2 = 2\pi/L_2$ and $k_1 = 2\pi/L_1$ represent the wave number above the elliptical lens and outside it, respectively. L_2 and L_1 represent the wavelength obtained in the depth above the lens (h_2) and outside the lens (h_1), respectively; e represents the eccentricity, which is determined from the relationship between the major semi axis a and the minor semi axis b as follows:

$$e = \sqrt{1 - \frac{b^2}{a^2}} \tag{1}$$

Therefore, for a given frequency and starting from a known depth h_1 and h_2, the authors determined the eccentricity necessary to obtain a wave convergence in the second geometrical focus of the elliptical lens. Their numerical results adequately described what was established by the conics refraction theory and demonstrated that elliptical lenses are more efficient than biconvex lenses. Thus, based on the conclusions of the work described above, and to find a suitable tool to focus wave energy, submerged elliptical structures were analyzed as they are more efficient than biconvex or Fresnel lenses, and also, to make use of the law of refraction in conics. However, there are still questions to be solved; for a known refractive index, determined by the change in depth between h_1 and h_2, there are innumerable possibilities to establish the eccentricity, since both the semi minor axis b and the semi major axis a, can take an infinity of values, as long as their proportion is always the same, to maintain the eccentricity constant. Inversely, from a known eccentricity, there are innumerable possibilities to establish the refractive index n, since h_1 and h_2 can take an infinite number of values, as long as they maintain their proportion constant to obtain the desired n. To solve this uncertainty, this article presents the numerical evaluation of the performance of submerged elliptical lenses for different geometric parameters, such as the eccentricity and the size of the semi-axes, as well as for different indices of refraction with respect to incident waves.

This paper is divided as follows, in section 2 the methodology used to carry out the numerical evaluation of the elliptical lens is described. This was carried out by means of a wave model of Boussinesq type, which was validated from laboratory tests in the wave basin of the Engineering Faculty of the UNAM (FI-UNAM). The results about the validation of the numerical model of Boussinesq as well as the numerical evaluation of the performance of the elliptical lens as a function of its geometrical parameters and the incident waves, are shown in section 3. Finally, in section 4 the most relevant conclusions of the present investigation.

Materials and methods

Numerical model

To carry out the numerical evaluation of the performance of the elliptical lenses, a wave model called CELERIS (Tavakkol & Lynett, 2017) was used, which solves the extended Boussinesq equations (Madsen & Sorensen, 1992). This type of equation solves the physical processes of refraction, diffraction, reflection, subjection and nonlinear interactions of waves in shallow water or in interaction with structures and is therefore suitable to solve coastal hydrodynamic processes (Nwogu, 1993; Kirby, 2003; Briganti, Musumeci, Bellotti, Brocchini& Foti, 2004), or interaction of waves with floating or submerged structures (Prinos, Avgeris, & Karambas, 2005; Fuhrman, 2005, Bingham, & Madsen, 2005; Soares & Mohapatra, 2015), and wave focusing processes (Tavakkol & Lynett, 2017). The numerical model was validated for different reference standard cases, such as wave run-up on slopes and conical islands, and wave focusing with circular geometries (Tavakkol & Lynett, 2017).

The equations involved are:

$$U_t + F(U)_x + G(U)_y + S(U) = 0 \tag{2}$$

$$= \begin{bmatrix} h \\ P \\ Q \end{bmatrix}, F(U) = \begin{bmatrix} P \\ \dfrac{P^2}{h} + \dfrac{gh^2}{2} \\ \dfrac{PQ}{h} \end{bmatrix}, G(U) = \begin{bmatrix} Q \\ \dfrac{PQ}{h} \\ \dfrac{Q^2}{h} + \dfrac{gh^2}{2} \end{bmatrix}, S(U) = \begin{bmatrix} 0 \\ ghz_x + \psi_1 + f_1 \\ ghz_y + \psi_2 + f_2 \end{bmatrix} \tag{3}$$

Where U is the vector of the conservative variables, $F(U)$ and $G(U)$ are the advective flow vectors and $S(U)$ is the source term that includes the dispersive terms, the friction and the information of the background changes. P and Q represent the average vertical flows x and y, respectively. The subscript x and y represent spatial differentiation and the subscript t denotes temporal differentiation. The water depth with respect to the vertical data is represented by z. f_1 and f_2 are the terms of background friction,, h is the total depth and g is the acceleration of gravity. The terms that express the dispersion are ψ_1y ψ_2 and are defined by:

$$\begin{aligned} \psi_1 = {} & -\left(B + \frac{1}{3}\right) d^2 \left(P_{xxt} + Q_{xyt}\right) - Bgd^3\left(\eta_{xxx} + \eta_{xyy}\right) \\ & - dd_x\left(\frac{1}{3}P_{xt} + \frac{1}{6}Q_{yt} + 2Bgd\eta_{xx} + Bgd\eta_{yy}\right) \\ & - dd_{yy}\left(\frac{1}{6}Q_{xt} + Bgd\eta_{xy}\right) \end{aligned} \tag{4}$$

$$\psi_2 = -\left(B + \frac{1}{3}\right) d^2 \left(P_{xyt} + Q_{yyt}\right) - Bgd^3 \left(\eta_{yyy} + \eta_{xxy}\right)$$

$$- dd_x \left(\frac{1}{3} Q_{yt} + \frac{1}{6} P_{xt} + 2Bgd\eta_{yy} + Bgd\eta_{xx}\right) \qquad (5)$$

$$- dd_{yy} \left(\frac{1}{6} P_{yt} + Bgd\eta_{xy}\right)$$

In which d is depth and $B = 1/15$ is the dispersion calibration coefficient. The free water surface is described by η.

Experimental design to validate the CELERIS model

For the evaluation of the model in simulating the focusing process with elliptical lenses, experiments were conducted in the FI-UNAM, in a rectangular concrete structure with a maximum capacity of 37.72m^3 of the following dimensions: 10.7 m long, 4.7 m wide and 0.75 m high (Figure 1). The swell was generated by a unidirectional, flap type paddle. A physical model of an elliptical lens with a semi-axis of less than 0.6 m, a half-axis greater than 1 m and a height of 0.122 m (Figure 2) was installed. A unidirectional monochromatic wave field was generated, with a frequency of 1.61 Hz and a height of 0.013 m. This was measured at the free surface, with resistive type level sensors. It should be noted that the dimensions of the elliptical lens were determined by numerical tests, where the semi-minor axis was fixed at the same value as the incident wavelength ($b = L_0$) and the heights and the semi-major axis were varied until a significant focus of the incident wave was found (when $a = 1.7L_0$). To control the reflection effects caused by the opposite wall to the wave paddle, a dissipative gravel beach (D50 = 0.025 m) was built with a slope of 1: 3 ratio. These array produced a reflection coefficient of less than 7 % for these wave conditions was obtained. This reflection coefficient is acceptable since it is below 10 % (Cotter & Chakrabarti, 1994). It should be noted that this coefficient was obtained by the 3-point method developed by Mansard and Funke (1980), with the modification to the least squares method proposed by Baquerizo (1995).

Figure 1. Rear view of the wave basin of the Hydraulics Laboratory of the Faculty of Engineering of the UNAM.

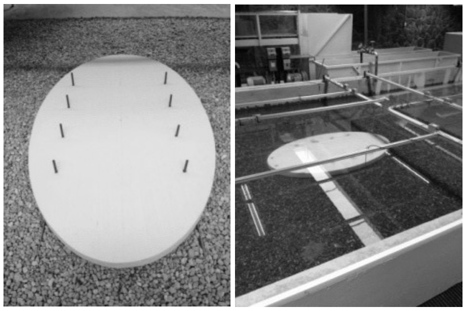

Figure 2. Elliptical lens mounted on the platform prior to the experiments.

To simulate the transition from deep to shallow water, a horizontal platform was constructed with the same material as the dissipative beach, with a height of 0.13 m above the tank bottom. The water level in all the experiments was 0.35 m.

To record the focusing process, 2 transects were instrumented (Figure 3), one on the optical axis (transect AB) and another transverse to the optical axis on the focal point (transect CD).

To measure the perturbed waves on one side of the elliptical lens, three transects were instrumented parallel to the optical axis at the height of the ellipse (transects EF, GH and IJ).

In order to verify the operation of the model for oblique waves, and because the paddle only generates unidirectional waves, the lens was turned 20 ° on the optical axis to simulate oblique incidence. In the lower panel of figure 3 a diagram of the position of the elliptical lens for oblique waves is shown, as well as the arrangement of the instruments which recorded changes in the focal area due to the change of the incident wave direction (KL and MN transects).

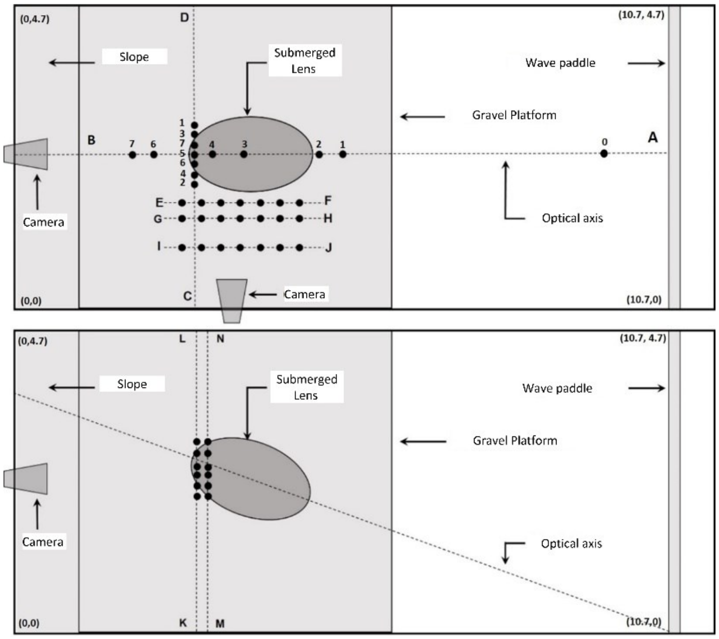

Figure 3. Diagram of the instrument arrangement for normal wave incidence (upper) and oblique (lower) incidence. The black dots represent the positions of the level sensors and the dotted lines represent the transects. The numbering in the upper panel indicates the comparison of the free surface and spectral time series.

The free surface sampling frequency of the sensors was 100 Hz (0.01 s) and the time length of the record was 120 s for each test. Figure 4 shows an example of two series recorded during the measurement period. From the free surface time series, the temporal analysis was carried out by means of the zero down crossing method, in order to obtain the statistical wave parameters, such as the height *H* and the period *T*. Subsequently, the mean square height (H_{rms}) was obtained, defined as:

$$\sqrt{-\sum} \qquad (6)$$

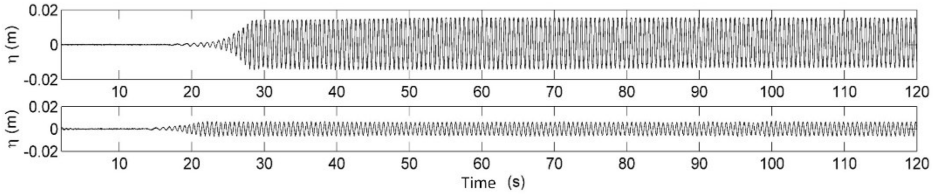

Figure 4. Free surface measurements from sensors AB5 (upper panel) y AB0 (lower panel).

Where is the total number of data and are the individual wave heights in the temporary record.

In order to compare the amount of energy of the incident wave, the focused wave, and the wave at a control point (corresponding to the position of the wave at the focal point but without the lens), energy spectra were evaluated by means of the Fast Fourier Transform (FFT); which, from the record of the free surface in the time domain, gives the amount of energy as a function of the frequency.

In addition to the surface level measurements recorded by the level sensors, the focusing process was recorded by means of a high-speed camera. The camera was installed in 2 positions, to record the side and front views of the focusing process (Figure 5). The video recording had a rate of 700 frames per second. Figure 5 shows a set of video frames for the case of normal incidence side view (upper panel) and front view (lower panel). For the case of side view, the waves travel from right to left, reaching a maximum in the focal area at 143 ms. In the front view, the transverse view of the lens is seen and the waves approach from back to front, reaching a maximum at 143 ms.

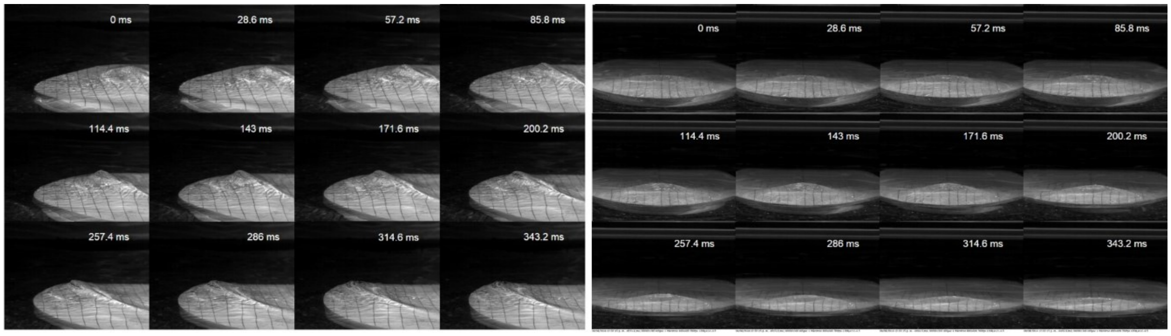

Figure 5. Video frames for the focalization process for normal incidence, side view (left panel) and front view (right panel).

Numerical basin

To obtain the simulated free surface with the CELERIS model, a numerical replica of the FI-UNAM installation was used. The numerical domain was divided into cells, 536 by 236 for the length (10.7 m) and width (4.7 m) of the basin, respectively, giving a rectangular mesh with a spatial resolution of 0.02 m (Figure 6). Wave generation in the numerical basin was simulated by means of a periodic sine-type function with an amplitude of 0.0066 m, a period of 0.62 s and an 0° direction (perpendicular to the optical axis of the elliptical lens), on the eastern border. The variables η, P and Q, are defined at the boundary as: $\eta = a \sin(wt - k_x x - k_y y)$; $P = c \cos \theta_\eta$ and $Q = c \cos \theta_\eta$. Where $c = w/k$; $w = 2\pi/T$; $k_x = \cos(\theta)k$ and $k_y = \sin(\theta)k$. The wave number k is defined using the following aproximation to the dispersion equation:

$$k = \frac{w^2}{g} \sqrt{\coth\left(\frac{w^2 d}{g}\right)} \tag{7}$$

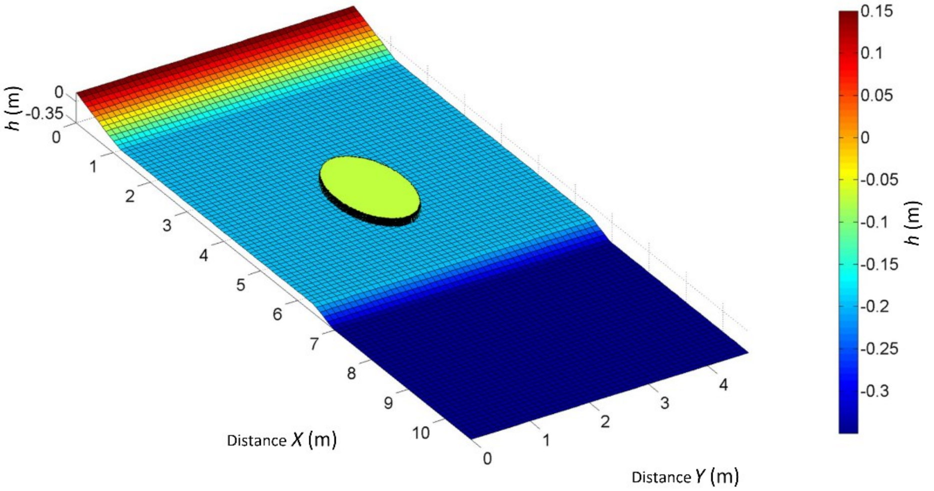

Figure 6. Schematic representation of the numerical basin used in the simulation of the focusing process with the CELERIS model. To visualize the discretization of the pond, each cell represents 5 cells of the numerical basin used.

To dissipate the wave energy and avoid reflection effects inside the numerical basin, the dissipative beach used in the physical modelling was replaced by a numerical sponge, which acts as a dissipation coefficient $\gamma(x, y)$ that multiplies the values of η, P and Q:

$$\gamma(x,y) = \frac{1}{2}\left(1 + \cos\left(\pi \frac{Ls - D(x,y)}{Ls}\right)\right) \tag{8}$$

Where *Ls* is the thickness of the sponge and *D (x, y)* is the normal distance to the absorbent boundary.

The side walls were considered totally reflective (as in the FI-UNAM), so that $(P, Q) \cdot \boldsymbol{n} = 0$; $\nabla w \cdot \boldsymbol{n} = 0$. Where ***n*** is the normal vector at the side wall of the numerical basin. The bottom friction in the model was given by the Manning roughness coefficient, obtained using the hydraulic radius R, the average size of the gravel (used in the FI-UNAM), of which 50 % of the rocks are smaller (D_{50}) and the average size of gravel of which 90% of rocks are smaller (D_{90}), by:

$$n = \frac{d_{90}{}^{1/6}}{26(1 - 0.3593^{x^{0.7}})} \tag{9}$$

For $x = (R/d_{90})(d_{50}/d_{90})$. The hydraulic radius *R*, was obtained from the ratio of the cross-sectional area of the basin between the "wet perimeter", which is the perimeter that is in contact with the water. From equation 9, a coefficient of *n* = 0.023 was obtained.

The integration time step of the model's governing equations was 0.001 s, and the acquisition of results was 100 Hz to homogenize the recording frequency of the simulated free surface with that obtained in the FI-UNAM. The simulation time was 30 s for all the experiments. With respect to the processing of numerical results, the same methodology was followed as that for the physical modeling. First, time series of the free surface were obtained in the same position and sampling frequency as the level sensors used in the FI-UNAM (Figure 2) and then the H_{rms} and energy spectra were obtained.

Results and discussion

The comparison of the free surface time series obtained with the CELERIS model and that of the experiments in the FI-UNAM, was made for a 10-second record, considering the 20 s as the beginning and 30 s as the end (Figure 7, left panel).

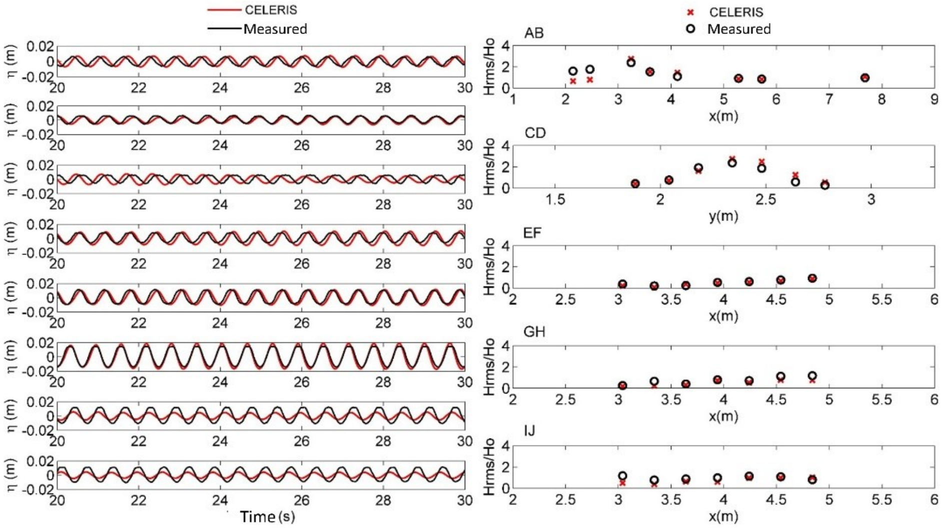

Figure 7. Left panel: Measured free surface data (black lines) and simulated, CELERIS model data (red lines). Right panel: Mean square heights: measured data (black circles) and CELERIS simulated data (red circles).

There was good agreement at the positions AB0, AB1, AB2, AB3, AB4 and AB5, but for the positions after the lens, AB6 and AB7, the model overestimated the measured data.

The positions that describe the focusing process on the lens are AB3, AB4 and AB5, where the latter has the greatest recorded amplitude. Positions AB2, AB1 and AB0, correspond to the positions before the lens.

For the evaluation of the elliptical lens performance, the most relevant information in the focalization process showed good agreement with the measured results (AB3, AB4 and AB5).

The standardized mean square height (H_{rms}/H_0) simulated on the transect AB, CD, EF, GH and IJ (figure 7, right panel), agreed well with the H_{rms}/H_0 obtained in the FI-UNAM, with the exception of the points after the submerged lens located at x =2.46 and x =2.14 m, where the model underestimated the measurements.

The transversal structure of the focal area (CD) was well represented by the model and the comparison of the waves in the lateral section to the lens (EF, GH and IJ) indicates that the model adequately represented the disturbed waves.

Figure 8 shows the comparison of H_{rms}/H_0 for the case of incident oblique waves, recorded in the KL and MN transects, which are positioned one behind the other, at a distance of 5 cm (Figure 2).

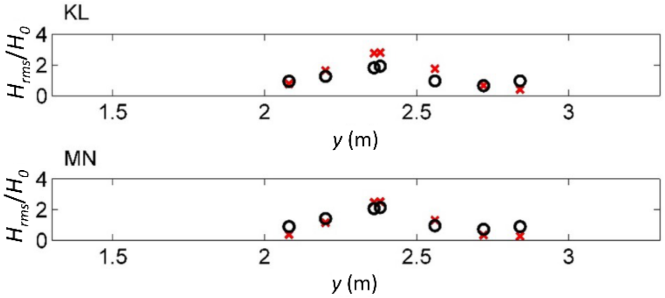

Figure 8. Comparison of the measured mean square height (black circles) and that simulated by the model (red crosses) on the KL and MN transects for the case of oblique incidence.

The comparison of H_{rms}/H_0, observed in Figure 8, indicates that the CELERIS model adequately solves the structure of the focus for oblique incidence. Subsequently, the energy spectra were obtained by means of the FFT corresponding to the AB transect on the optical axis (Figure 9) and to the transect CD transverse to the optical axis on the focal point (Figure 10). It can be observed in Figure 9, that the energy spectra are similar for the positions AB0, AB1, AB2, AB3, AB4 and AB5, where this last point represents the focal point. However, in the case of points AB6 and AB7, the energy obtained from the CELERIS data was lower than that obtained from the recorded data.

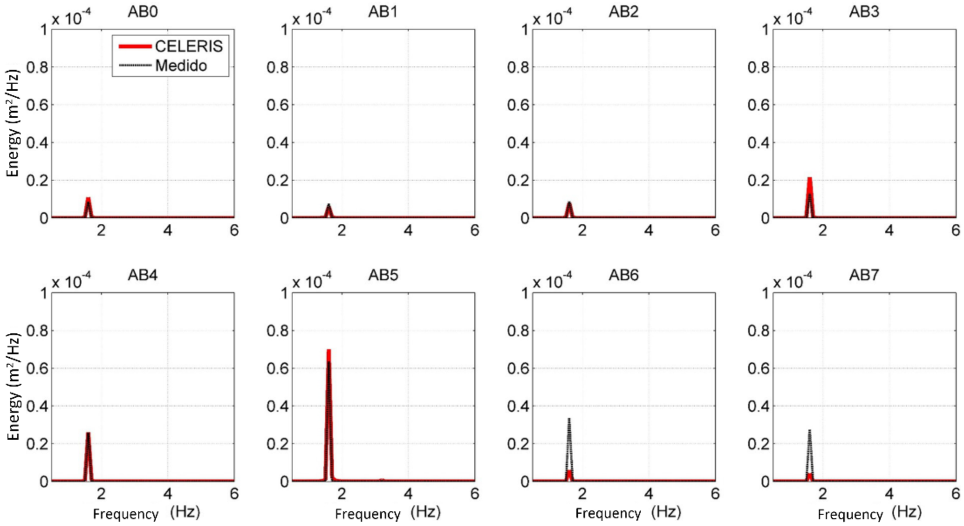

Figure 9. Comparison of the energy spectra obtained by means of simulations with the CELERIS model (red line) and from the recorded measurements (black line) on the AB transect.

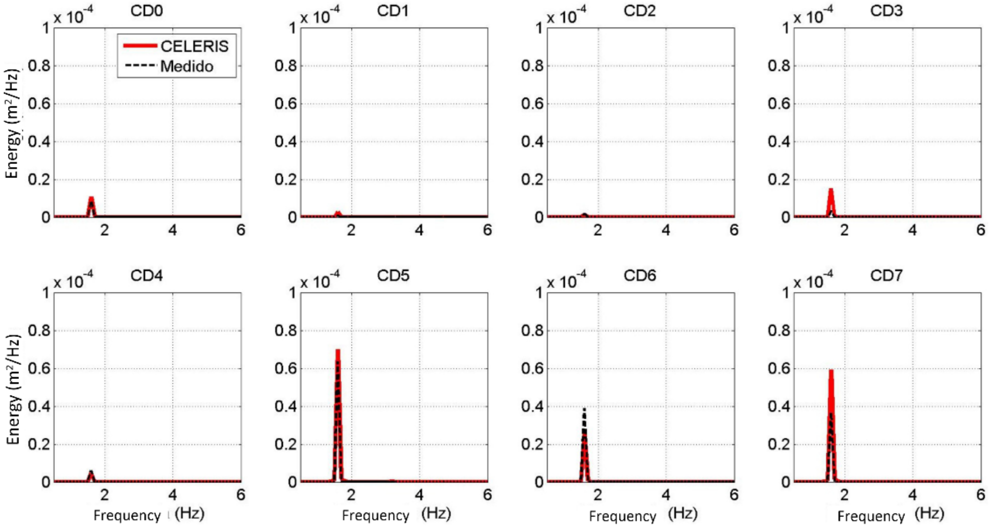

Figure 10. Comparison of the energy spectra obtained by means of CELERIS simulations (red line) and from that recorded in the FI-UNAM (black line) on the CD transect.

The comparison made by means of the free surface, the H_{rms}/H_0 and the energy spectra, indicate that the CELERIS model adequately solves the focusing process for monochromatic waves and waves with normal and oblique incidence. It should be noted that despite the underestimations found in AB6 and AB7, the model correctly solved the focalization process in strategic positions, such as the focal area and the area before the elliptical lens, positions from which the performance evaluations of the submerged lens were made, as described below.

Evaluation of the submerged lens performance

In order to standardize the performance tests in a reference parameter corresponding to the incident waves, the water depth, determined by the depth between the submerged lens and the water mirror h_1, the total depth in which the lens is submerged, h_2, determined by the depth between the free water surface and the depth of the platform on which the lens is positioned, and the eccentricity of the lens *e*, determined by the semi minor axis *b* with respect to the semi major axis *a*, were related to fractions of L_0.

To obtain a comparison of the amplification of the energy, the spectrum was obtained for each test, at the focal point of the incident wave (at *x* = 8 m and *y* = 2.35 m) and at the control point. The focal point was defined as the location where the maximum H_{rms} was found on the optical axis for each test. The border conditions that were used in these experiments were the same as those used for the validation of the numerical model, where a height of 0.013 m, a period of 0.62 s and a propagation direction θ of 0° were imposed (except for the approach direction tests where θ was variable).

Because the waves in the basin can behave like a set of quasi-stationary waves (Dean & Darymple 1984), it is very important to know the influence of the reflected waves in the focusing process, especially if the experiments are prolonged (Cotter & Chakrabarti, 1994).

To know the influence of the energy reflected by the lateral walls of the numerical basin, two tests lasting 30 s were carried out in a basin with the lateral walls far away and in the basin validated for the same boundary conditions, to determine a window of time where the focus is not affected by reflection. Figure 11 shows the profile of H_{rms} on the corresponding optical axis for a time range of 14 s to 19 s (when focusing begins) and from 25 s to 30 s.

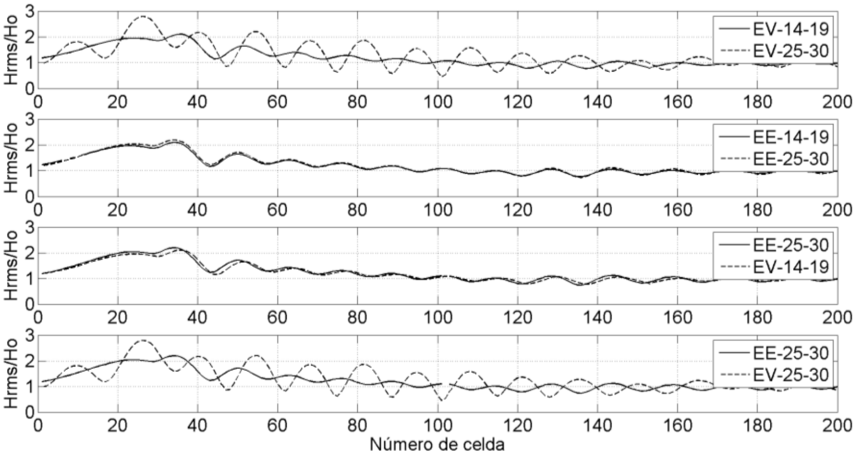

Figure 11. Profiles of for the validated basin (EV) and Extended Basin (EE) tests.

It can be seen that for the case of the validated basin (EV, first panel) there are significant differences in the profile of H_{rms} between 14s and 19s and between 25s and 30s unlike the extended basin (EE, second panel) where the profiles are the same for these ranges. The profile of H_{rms} for the validated basin and the extended basin for 14s and 19s and for 25s and 30s, respectively, are similar to each other (third panel). Thus all the performance tests were evaluated for the 14s to 19s interval in the validated basin.

Effects of the relative water depths of the submerged lens

The purpose of these tests was to evaluate the performance of the elliptical lens for different relations between h_2 and h_1 with a constant h_1 to determine a ratio that gives maximum focalization of energy.

The platform on which the elliptical lens was mounted was fixed at a height of 0.15 m above the bottom of the numerical basin so that h_1 was 0.20 m. The L_0, with which the height increase of the elliptical lens was normalized, was 0.583 m (3% less than the deep water wavelength of 0.6 m). The eccentricity of the lens remained fixed at the same value as in the validation tests (0.8). It should be noted that the depth at which the elliptical lens was installed was 1/3 L_0. Table 1 shows the list of tests to determine the water depth (TA). Figure 12 shows the energy spectra obtained at the focal point for each of the tests, as well as that for the incident wave and at the control point. It can be observed that the energy of the incident wave and at the control point is similar, with the incident energy being slightly higher, because it was not affected by background effects.

Table 1. Position of the focus generated for different water strains. The obtained H_{rms} is shown, as well as the refractive index n and the absolute distance between the numerical focus and the geometric δ. In the case of WD1 and WD2, no defined focus was generated.

Test		**L_0 factor**	**Pos. x (m)**	**H_{rms} (m)**	**n**	**δ (m)**
WD1		1/3	n/a	0.0119	1.003	n/a
WD2		¼	n/a	0.0170	1.049	n/a
WD3		1/5	3.38	0.0231	1.104	0.02
WD4		1/6	3.38	0.0283	1.161	0.02
WD5		1/7	3.38	0.0317	1.219	0.02
WD6		1/8	3.38	0.0324	1.276	0.02
WD7		1/9	3.38	0.0306	1.332	0.02
WD8		1/10	3.62	0.0312	1.387	0.22

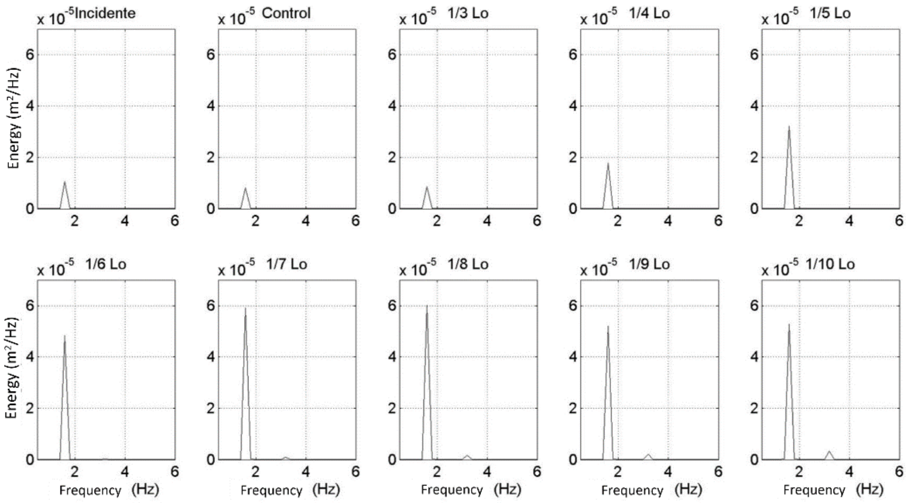

Figure 12. Energy spectra of the focalized wave for different water depths on the elliptical lens. The spectrum of the incident and control waves is shown.

As the water depth on the elliptical lens begins to decrease, the energy increases up to a maximum point in a depth of 1/8 L_0. Then, towards the depth of 1/9 L_0 and 1/0 of L_0, this energy begins to decrease. With respect to the incident energy and with the control point calculated, it can be seen that for the elliptical lens submerged at depths of $1/7L_0$ and $1/8L_0$, the focalized energy is approximately 6 and 7 times greater respectively, with $1/8L_0$ being the optimal depth.

For depths of $1/5L_0$, $1/6L_0$ and $1/10L_0$, the focalized energy is slightly more than twice that simulated at the control point. For the cases of $1/3L_0$ and $1/4L_0$ no considerable amplification is seen, since for these depths the waves have little interaction with the lens. Indicating the first range of applicability of the law of refraction of conics. It can be observed in Table 1, that the refractive index n for the case of maximum amplification in (1/8 of L_0), is approximately the inverse of the eccentricity of the submerged lens (1/*e* = 1.25), coinciding with the law of refraction of conics (Griffiths & Porter, 2011).

Eccentricity tests

Taking the numerical pre-tests, mentioned in the methodology, the semi major axis (*a*) remained fixed at a size of $1.7L_0$ and the semi minor axis (*b*), adopted different sizes in L_0 factors. For this case, 8 eccentricities were taken into account, which were obtained by multiplying *b* by various factors of L_0, ranged between $3/2L_0$ to 1/4 L_0. Table 2 shows the set of numerical simulations that were performed, termed LE (Lens Eccentricity). The refractive index n had a fixed value of 1.276. In Figure 13, the eccentricities that were used for the numerical design of each elliptical lens of each experiment were schematized. The ellipse with an eccentricity of 0.784 is that determined from the law of conic refraction. The geometric focus of each of the elliptical lenses is shown.

Table 2. Position of the generated focus for different eccentricities. The obtained H_{rms} is shown in said focus, as well as the refractive index n and the absolute distance between the numerical focus and the geometric focus δ.

Test	**Factor L_0**	e	**Pos. x (m)**	H_{rms} **(m)**	δ **(m)**
LE1	1.500	0.484	3.140	0.0325	0.58
LE2	1.064	0.784	3.380	0.0329	0.02
LE3	1.000	0.811	3.380	0.0322	0.02
LE4	0.875	0.859	3.380	0.0309	0.04
LE5	0.750	0.899	3.380	0.0297	0.08
LE6	0.500	0.956	3.440	0.0295	0.18
LE7	0.375	0.975	3.440	0.0290	0.22
LE8	0.250	0.989	3.700	0.0247	0.43

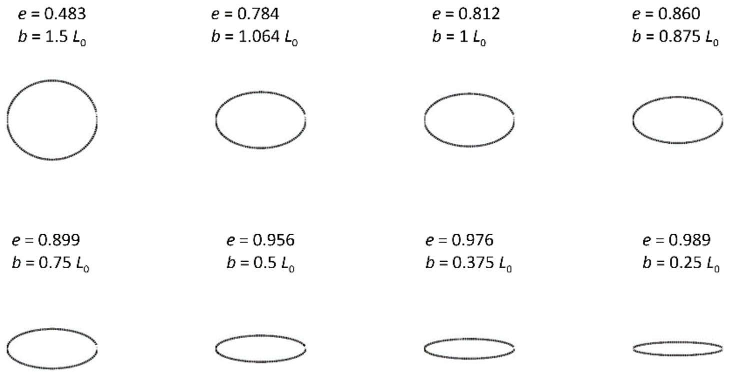

Figure 13. Different lens eccentricities for the numerical simulations. The eccentricity value (e) and the factor of L_0 by which the minor semi axis (b) was multiplied are shown.

In Figure 14, LE1, LE2 and LE3 are seen to have the highest amounts of concentrated energy, with values close to 6 times the incident energy and almost 8 times the energy observed at the control point. LE2 has the greatest increase. From LE4 the energy begins to decrease as the eccentricity increases until reaching the case of LE8.

It is important to note that in the tests of water depths and eccentricity, the cases determined by the law of conic refraction, are those that have most increased energy. For the case of water depth on the elliptical lens, the ratio of k_2/k_1, determined by the change in the height of the lens, was approximated to the inverse of the eccentricity of the lens in the tests.

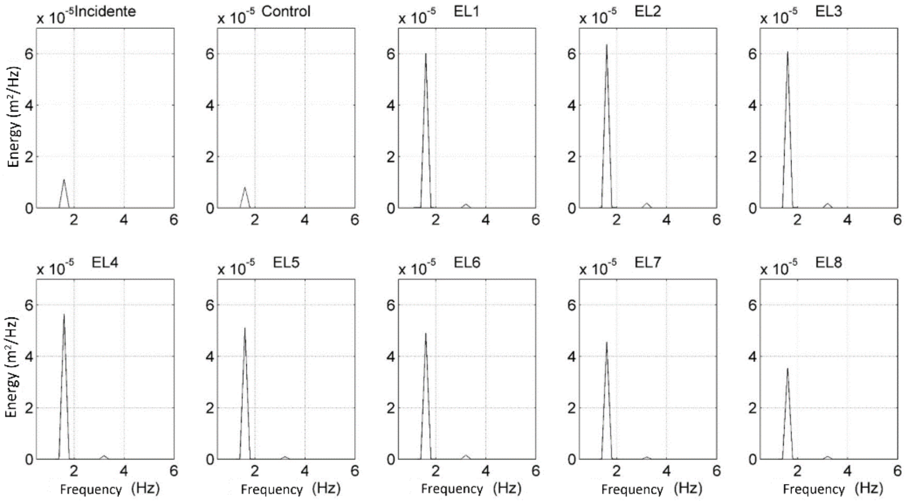

Figure 14. Energy spectra of the focalized wave for different eccentricities. The spectrum of the incident and control waves is shown.

For the case of the eccentricity tests, the eccentricity of the LE2 case was exactly the inverse of k_2/k_1. It was also the case where most energy amplification was produced of all the tests (more than 6 times the incident energy and almost 8 times the energy at the control point). Given the above, and in order to optimize the size of the lens, tests were performed for a constant eccentricity, determined by the law of conic refraction, but proportionally decreasing the semi minor axis (*b*) and the semi major axis (*a*). For this case, *b* was reduced by factors of the L_0, from $1L_0$ to $0.25L_0$, every $0.25L_0$ and a was obtained from equation 1 for a constant eccentricity and the corresponding value of the minor semi axis. In Figure 15 the sizes of the elliptical lenses with constant eccentricity of 0.784 for the tests are shown. The geometric focus and the center of each of the elliptical lenses are shown.

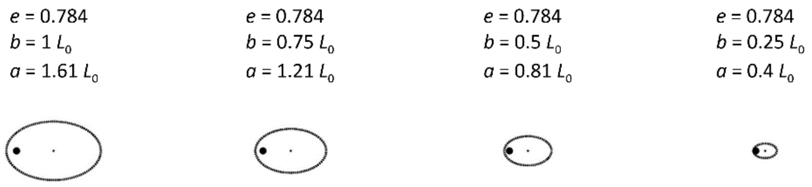

Figure 15. Schematization of the elliptical lenses used for the size optimization for a constant eccentricity of 0.784, obtained from the law of conic refraction.

Table 3 shows the position of each focus on the optical axis, the H_{rms} obtained in this position and the absolute distance between each focus found and the geometric focus of the ellipse (δ). Each test was labelled with the acronym EC de noting Constant Eccentricity. It should be noted that as the size of the lens in these tests was reduced, the upper area of the lens was added in Table 3 for comparative purposes. It can be observed in Table 3 that δ is similar for EC1 and EC2, while for EC3 and EC4, it increased considerably, indicating that despite maintaining the constant eccentricity of 0.784, there is a limit in the size reduction for the law of conic refraction to produce the expected results, where b>=3/4L_0.

Table 3. Position of the focus generated for the different sizes of the lens with constant eccentricity. The average quadratic height obtained in the focus is shown, as well as the size of the semi axes *a* and *b*, the area of the lens and the absolute distance between the numerical focus and the geometric focus δ.

Test	L_0 factor (b)	a(m)	b(m)	Area (m2)	H_{rms} (m)	δ (m)
EC1	1.000	0.940	0.584	1.72	0.0330	0.02
EC2	0.750	0.705	0.438	0.97	0.0329	0.02
EC3	0.500	0.470	0.293	0.43	0.0276	0.08
EC4	0.250	0.235	0.146	0.11	0.0181	0.14

Figure 16 shows the energy spectra obtained for each of the tests mentioned in Table 3, as well as for the incident wave and at the control point.

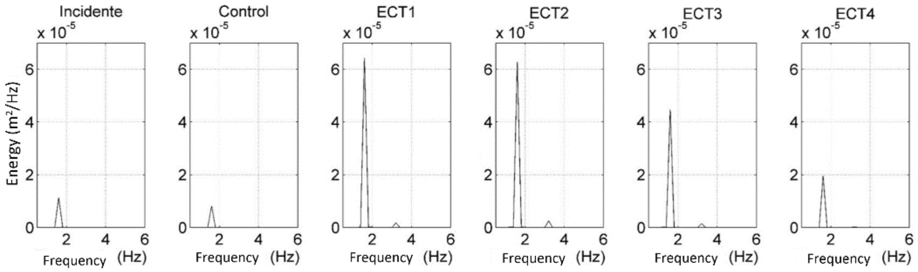

Figure 16. Energy spectra of the focalized wave for different sizes of elliptical lens for a constant eccentricity of 0.784. The spectrum of the incident and control waves is shown.

It can be observed in Figure 16 that despite the difference in size of the elliptical lenses corresponding to EC1 and EC2, both amplify approximately the same amount of energy, indicating that EC2 (with a semi axis of $3/4L_0$) with an area about half that of EC1, amplifies practically the same amount of energy. Thus, EC2 is a more viable, optimized option than EC1. It should be noted that the focal area produced by EC1 and EC2 are very similar to each other, despite the difference in size of the lens, as shown in Figure 17, where a comparison of the maximum free surface is shown as a snapshot for EC1 and EC2. The dotted lines delimit the same contours of both cases, indicating that the size of the focus is similar for both. As the lens begins to decrease in size towards EC3 and EC4, the energy amplification becomes decreases, to where, in the case of EC3, the lens is almost transparent for the incident wave.

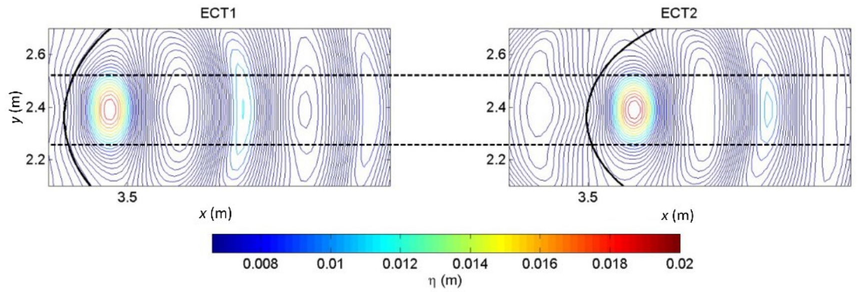

Figure 17. Wave amplitude and comparison of the size of the focal area produced by the lens of EC1 (left panel) and EC2 (right panel).

Tests of the total depth

In order to know how much the focusing process is affected by the elliptical lens with respect to the total depth in which it is submerged, several numerical simulations were performed for different depths. Table 4 shows the list of tests performed. Each test was given the acronym PP denoting Platform Depth. As can be seen in Table 4, for PP2, δ increased considerably, indicating that despite maintaining the eccentricity defined by the law of conic refraction, there is a limit on the reduction of h_1 so that the conic refractive law continues to give the results expected, where $h_1 <= 1/3 L_0$.

Table 4. Position of the focus generated for the depth tests. The average quadratic height obtained at the focus, the refractive index n, the eccentricity e and the absolute distance between the numerical focus and the geometric focus δ are shown.

Test	h_1 **(m)**	n	e	**Position (m)**	H_{rms} **(m)**	δ **(m)**
PP1	0.150	1.225	0.816	3.64	0.0284	0.02
PP2	0.100	1.109	0.902	3.50	0.0230	0.08

Figure 18 shows the energy spectra obtained for each of the tests mentioned in Table 4, as well as for the incident wave and at the control point.

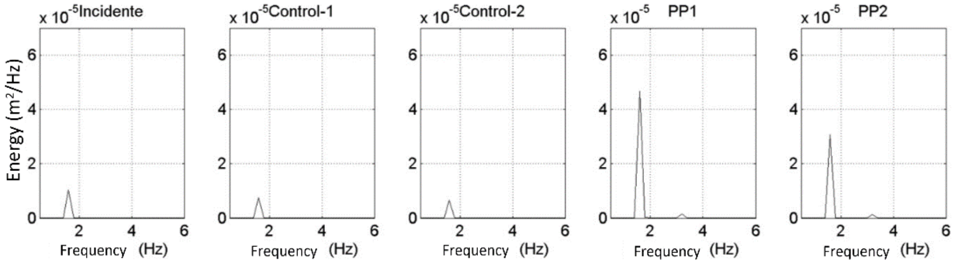

Figure 18. Energy spectra of the focalized wave for different depths and for different eccentricities obtained for each depth. The spectrum of the incident wave and control-1 and control-2 corresponding to tests PP1 and PP2, respectively, are shown.

The amplified energy for the case of PP1 was 4 times and 6 times with respect to the incident energy and the control point, respectively. For the case of PP2, it was 4 and 3 times with respect to the concentrated energy with respect to the incident energy and the control point, respectively, indicating that despite maintaining the eccentricity defined by the law of conic refraction, there is an important impact when the depth to which the lens is submerged is decreased, since for depths of the order of $1/3L_0$ the incident energy and at the control point was amplified approximately 6 times and 8 times, respectively (case EC2).

Tests of change in the direction of the incident wave

Three tests were performed corresponding to angles of incidence with respect to the optical axis of 10°, 20° and 30°. To simulate the change in the angle of incidence, the elliptical lens was turned 10°, 20° and 30° clockwise. For each case, the instantaneous maximum free surface was graphed and the corresponding energy spectra were obtained at the point of maximum amplification.

Table 5 shows the cases evaluated where the angle of incidence and the position of the maximum are specified in x, y coordinates. Each test was given the acronym LED denoting Elliptical Lens Direction.

Table 5. Position of the focus generated for the direction tests. The average quadratic height obtained in the focus in coordinate pairs and the angle of incidence of the wave with respect to the optical axis is shown.

Test	Angle	Focus position (X,Y)
LED1	10°	(3.68,2.44)
LED2	20º	(3.68,2.44)
LED3	30º	(3.72,2.44)

Figure 19 shows the position of the focus for each of the cases evaluated, where the optical axis is indicated so as to have a reference of the change of position.

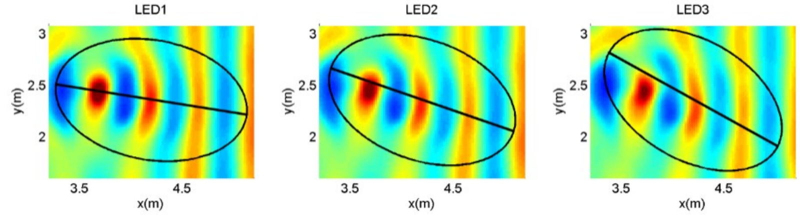

Figure 19. Maximum instantaneous free surface for 10° (ELD1, left panel), 20° (LED2, middle panel) and 30° (LED3, right panel).

Figure 20 shows the spectra obtained at the positions indicated in Table 5, as well as the spectrum of the incident wave and at the control point. It can be observed in Figure 19 that as the angle of incidence of the waves increases, the focus moves to one side of the optical axis and the amount of energy concentrated by the lens decreases, from 5-6 times, and to 4 times and 6-7 times and 5 times the energy obtained at the control point, for LED1, LED2 and LED3, respectively (see figure 20). The change of the position of the focus with respect to the optical axis was recorded by high-speed video in the FI-UNAM for the case of an angle of incidence of 20° (corresponding to LED2) and the displacement of the focal area coincides with the that was simulated with the CELERIS model (Figure 21).

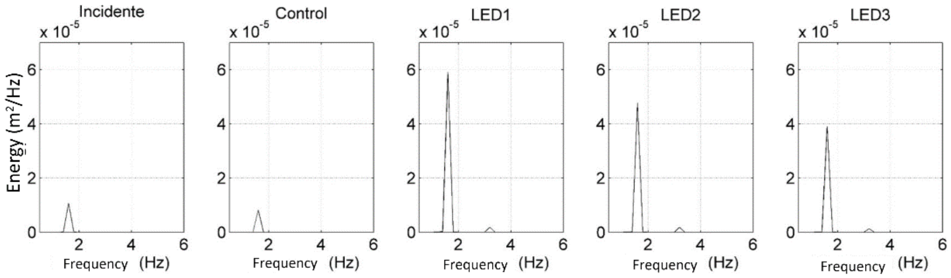

Figure 20. Focused wave energy spectra for different angles of wave incidence (10° LED1, 20° LED2 and 30° LED3). The spectrum of the incident and control waves is shown.

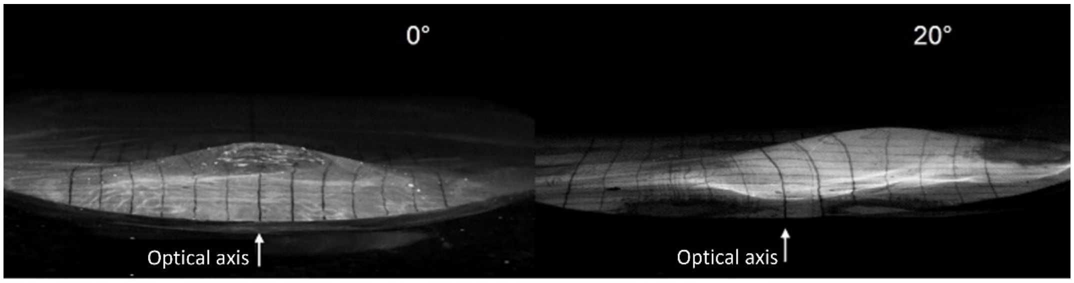

Figure 21. Video frames of the free surface for 0° (left panel) and 20° (LED2, right panel).

Conclusions

In this research the ability of submerged elliptical lenses to amplify wave energy that could be harnessed as a source of renewable energy was evaluated through numerical simulations with a Boussinesq type model. The CELERIS model was satisfactorily validated by means of laboratory tests in the FI-UNAM, showing that it is capable of simulating the focalization process adequately for waves with normal incidence and those with oblique incidence. With respect to the performance evaluation tests, it was found that with the geometries defined from the refractive index and/or the resulting eccentricity of the conics refractive law, the greatest amount of energy was obtained in the focal point, where the energy calculated obtained was between 7 and 8 times that at the control point. However, it was found that there are certain limits of water depth, installation depth and size of the respective semi-axes to L_0 so that from the conic refraction law the expected results are obtained; since for a water depth of more than $1/5L_0$ the lens is practically invisible to the incident wave, and for a depth of less than $1/4L_0$, the focus position differs significantly from the geometric focus and the concentrated energy decreases considerably. The best results were found for a minor axis of the order of $3/4L_0$, a water line of the order of $1/8L_0$, and an installation depth of the order of $1/3L_0$ (EC2). The change in the position of the focus and the amount of concentrated energy varied significantly with respect to the change of direction of the incident wave, where for a 30° angle of incidence, the reduction of the energy concentrated by the elliptical lens was approximately 35% (ELD3) with respect to the concentrated energy when the wave incidence is normal to the optical axis (CE2).

This article establishes optimal ranges for the design of a submerged elliptical lens from the incident wavelength, with which an energy concentration can be obtained which is approximately 8 times greater (during stable conditions) than without a submerged lens (point of control). In addition, lens performance metrics for different geometries are suggested, in terms of eccentricity and height, as well as depth of installation, thereby offering different alternatives.

Acknowledgements

For the financing of the development of this project, the CONACyT is thanked. Conacyt-Sener Fund (project ICCEO-232986) were responsible for partial financing, during the numerical simulations of the CELERIS model. The authors wish to thank Ing. Ponciano Trinidad Ramírez for support in the laboratory testing.

References

Baquerizo, A. (1995). *Reflexión del oleaje en playas. Métodos de evaluación y predicción* (tesis doctoral). Santander, España: Departamento de Ciencias y Técnicas del Agua y del Medio Ambiente, Universidad de Cantabria.

Briganti, R., Musumeci, R. E., Bellotti, G., Brocchini, M., & Foti, E. (2004). Boussinesq modeling of breaking waves: Description of turbulence. *Journal of Geophysical Research*, 109, C07015, 1-17.

Cotter, C. D., & Chakrabarti, K. S., (1994). Comparison of wave reflection equations with wave-tank data. *Journal of Waterway, Port, Coastal, and Ocean Engineering*, 102(2), 226-232.

Dean, R. G., & Dalrymple, R. A. (1984). *Water wave mechanics for engineers and scientists*. New York, USA: Prentice-Hall.

Fuhrman, D. R., Bingham, H. B., & Madsen, P. A. (2005). Nonlinear wave-structure interactions with a high-order Boussinesq model. *Coastal Engineering*, 52(8), 655-672.

Griffiths, L. S., & Porter, R. (2011). Focusing of surface waves by variable bathymetry. *Applied Ocean Research*, 34, 150-163.

Kirby, J. T. (2003). Boussinesq models and applications to nearshore wave propagation, surf zone processes and wave-induced currents. *Elsevier Oceanography Series*, 67, 1-41.

Madsen, P. A., & Sorensen, O. R. (1992). A new form of the Boussinesq equations with improved linear dispersion characteristics. Part 2: A slowly-varying bathymetry. *Coastal Engineering*, 18, 183-204.

Mansard, E. P. D., & Funke, E. R. (1980). The measurement of incident and reflected spectra using a least squares method. Procedures (pp. 154-172). *17th Conference on Coastal Engineering*, Sydney, Australia.

Mehlum, E., & Stamnes, J. (1978). On the focusing of ocean swells and its significance in power production (pp. 1-38) (SI Rep. 77). Bliundern, Oslo, Norway: Central Institute for Industrial Research.

Murashige, S., & Kinoshita, T. (1992). An ideal wave focusing lens and its shape. *Applied Ocean Research*, 14, 275-90.

Nwogu, O. (1993). Alternative form of boussinesq equations for nearshore wave propagation. *Journal of Waterway, Port, Coastal and Ocean Engineering*, 119(6), 618-638.

Prinos, P., Avgeris, I., & Karambas, T. (2005). *Low-crested structures: Boussinesq modeling of waves propagation. Environmentally Friendly Coastal Protection*. NATO Science Series. Series IV: Earth and Environmental Series, 53. Dordrecht, The Netherlands: Springer.

Soares, G. C., & Mohapatra, C. S. (2015). *Wave forces on a floating structure over flat bottom based on Boussinesq formulation. Renewable Energies Offshore*. London, UK: Taylor and Francis Group.

Stamnes, J. J., Lovhaugen, O., Spjelkavik, B., Chiang, C. M. L. E., & Yue, D. K. P. (1983). Nonlinear focusing of surface waves by a lens - theory and experiment. *Journal of Fluid Mechanics*, 135, 71-94.

Tavakkol, S., & Lynett, P. (2017). Celeris: A GPU-accelerated open source software with a boussinesq-type wave solver for real-time interactive simulation and visualization. *Computer Physics Communications*, 217, 117-127.